Beneficial redox activity of halide solid electrolytes empowering high-performance anodes in all-solid-state batteries

Cheng, Zhu; Zhao, Wenxuan; Wang, Qidi; Zhao, Chenglong; Lavrinenko, Anastasia K.; Vasileiadis, Alexandros; Landgraf, Victor; Bannenberg, Lars; Li, Yuhang; Liang, Junwei

DOI
10.1038/s41563-025-02296-6

Publication date
2025

Document Version
Final published version

Published in
Nature Materials

Citation (APA)
Cheng, Z., Zhao, W., Wang, Q., Zhao, C., Lavrinenko, A. K., Vasileiadis, A., Landgraf, V., Bannenberg, L., Li, Y., Liang, J., Liu, M., Ganapathy, S., & Wagemaker, M. (2025). Beneficial redox activity of halide solid electrolytes empowering high-performance anodes in all-solid-state batteries. *Nature Materials*, *24*(11), 1763-1772. https://doi.org/10.1038/s41563-025-02296-6

nature materials

Article

https://doi.org/10.1038/s41563-025-02296-6

Beneficial redox activity of halide solid electrolytes empowering high-performance anodes in all-solid-state batteries

Received: 5 April 2024

Accepted: 19 June 2025

Published online: 16 July 2025

Check for updates

Zhu Cheng[1], Wenxuan Zhao[1], Qidi Wang[1], Chenglong Zhao[1], Anastasia K. Lavrinenko[1], Alexandros Vasileiadis[1], Victor Landgraf[1], Lars Bannenberg[1], Yuhang Li[2], Junwei Liang[2], Ming Liu[2], Swapna Ganapathy[1] & Marnix Wagemaker[1]

All-solid-state batteries receive ample attention due to their promising safety characteristics and energy density. The latter holds true if they are compatible with next-generation high-capacity anodes, but most highly ion-conductive solid electrolytes decompose at low operating potentials, leading to lithium loss and increased cell resistances. Here the dynamic stability of solid electrolytes that can improve all-solid-state battery performance is demonstrated. Halide electrolytes $Li_3YCl_3Br_3$ and Li_2ZrCl_6, considered unstable at low potentials, are found to exhibit structurally reversible redox activity beyond their electrochemical stability windows, increasing compatibility with anodes and contributing to capacity without compromising ionic conductivity. The benefit of this dynamic stability window is demonstrated with cost-effective red phosphorus anodes, resulting in high reversible capacities (2,308 mAh g^{-1}), high rate capacity retention (1,024 mAh g^{-1} at 7.75 mA cm^{-2}) and extended cycle life (61% retention after 1,780 cycles). Furthermore, high areal capacity (7.65 mAh cm^{-2}) and stability (70% retention after 1,000 cycles) are achieved for halide-based full cells with red phosphorous anodes. The beneficial redox activity of halide electrolytes greatly expands their application scenarios and suggests valuable battery design principles to enhance performance.

All-solid-state batteries (ASSBs) have attracted great interest due to their enhanced safety and potential for high energy density when paired with low-potential and high-capacity anodes[1]. The development of highly conductive solid electrolytes (SEs), particularly sulfide and halide types, has enabled fast Li-ion transport in solid-state systems[2]. Sulfide SEs, although offering excellent ionic conductivity and mechanical properties[3], suffer from narrow electrochemical stability windows and interfacial degradation that limit long-term cycling performance[4–6]. Halide SEs have emerged as promising alternatives, combining high ionic conductivities with superior oxidation stability due to halogen chemistry[7,8]. However, they remain vulnerable to reduction at the anode–SE interface, forming electronically conductive products that deteriorate cell performance[9]. To address this, sulfide–halide hybrid configurations have been proposed, leveraging the kinetic stability of sulfides near the anode and halide stability near the cathode. Yet, chemical incompatibilities at their interface often lead to new failure modes[10,11]. This underscores that one of the primary challenges for developing high-performance ASSBs remains establishing stable and Li-ion conductive interfaces between the electrodes and SEs.

[1]Section Storage of Electrochemical Energy, Radiation Science and Technology, Faculty of Applied Sciences, Delft University of Technology, Delft, The Netherlands. [2]Shenzhen Key Laboratory of Power Battery Safety and Shenzhen Geim Graphene Center, Tsinghua Shenzhen International Graduate School, Tsinghua University, Guangdong, China. e-mail: m.wagemaker@tudelft.nl

To establish a perspective on the development of electrode–SE interfaces, it is insightful to consider different decomposition scenarios that can occur. Traditional thermodynamic predictions of SE stability, which are based on the formation energies of decomposition products[5,12,13], often underestimate the observed electrochemical window because actual decomposition may proceed through intermediate (de)lithiated states rather than direct decomposition[14,15]. For instance, argyrodite Li_6PS_5Cl (LPSC) undergoes oxidation via delithiated intermediates ($Li_{6-x}PS_5Cl$), mediated by its sulfur redox, before decomposing into Li_3PS_4, LiCl and S—consistent with the observed potentials[16]. Consequently, argyrodite SEs can operate over a wider practical voltage window, contribute to initial capacity and potentially enable reversible sulfur redox during cycling[15,16], but at the cost of poor conductivity and chemomechanical stability, which remain performance-limiting factors.

Another scenario involves reversible SE (de)lithiation before decomposition, thus maintaining structural integrity, as observed in $Li_{1.5}Al_{0.5}Ti_{1.5}(PO_4)_3$ (refs. 14,17). It is interesting to consider whether such reversible SE redox activity could deliberately be used to benefit ASSB performance. To be beneficial, two conditions must be met: first, electrode working potentials must fall within the SE's reversible redox window to avoid detrimental decomposition and potentially contribute to additional reversible anode capacity; second, key SE properties, particularly Li-ion conductivity, should not be compromised during redox reactions. Whereas decomposition typically produces low-conductivity products and causes contact loss through volume changes, structural maintenance of the SE during (de)lithiation may alter conductivities without necessarily compromising performance. Enhanced Li-ion conductivity of the SE lowers the internal resistance, whereas enhanced electronic conductivity will allow it to activate more SE redox capacity further away from the electrode surface. However, uncontrolled enhancement of the SE electronic conduction into the separator region could promote decomposition, dendrite growth or even a short-circuit.

Here we explore the dynamic stability concept, and how the reversible redox activity of the SE can be turned beneficial for ASSB performance. Halide SEs, such as $Li_3YCl_3Br_3$ (LYCB), crystallize in layered structures analogous to layered oxide cathodes (for example, $LiCoO_2$)[18,19], suggesting potential for reversible (de)lithiation. We show that LYCB undergoes reversible lithiation down to 0.2 V versus Li/Li^+—well below its thermodynamic reduction limit (0.62 V versus Li/Li^+)—supported by density functional theory (DFT) calculations, thereby providing a wider operation window. This redox activity offers capacity (84 mAh g^{-1} from LYCB to $Li_{4.43}YCl_3Br_3$) and enhances Li-ion conductivity, as verified by electrochemical impedance spectroscopy (EIS) and related distribution relaxation time (DRT) analyses. Leveraging this beneficial redox behaviour, we enable highly reversible cycling of a cost-effective, low-potential and high-capacity red phosphorus (RP) anode in LYCB-based half-cells, whose operating voltage falls within LYCB's dynamic stability window. Furthermore, the compatibility of LYCB with both low- and high-voltage electrodes allows the realization of 'single-halide-based' full cells (uncoated $LiCoO_2$ (LCO)/$LiNi_{0.8}Mn_{0.1}Co_{0.1}O_2$ (NMC)|LYCB|RP) that exhibit a long cycle life (1,000 cycles) and high areal capacities (7.65 mAh cm^{-2}) at room temperature. To underline the generality of the beneficial redox activity of SEs, it is also demonstrated for trigonal Li_2ZrCl_6 (LZC) SE, bringing forward how SEs can actively contribute to ASSB performance when applied to both anodic and cathodic mixtures. The discovered redox activity of halide SEs expands their application scenarios in which the SE takes an active role in the design of high-performance electrode–SE interfaces in ASSBs.

Redox activity of LYCB

To enhance the redox reaction interface area, LYCB is ball milled with carbon nanofibres (CNFs), and the resulting LYCB-CNF's electrochemical performance is evaluated in a Li-In|LYCB|LYCB-CNF cell. Cyclic voltammetry (CV) results (Fig. 1a) reveal a pronounced cathodic current around 1 V versus Li/Li^+ during the initial negative scan, with multiple peaks corresponding to the stepwise reduction of Y^{3+}. The cathodic current rapidly increases to 1 mA cm^{-2} at 0 V versus Li/Li^+, consistent with the galvanostatic discharge profile, which shows an extended plateau at 0.1 V versus Li/Li^+, exceeding the theoretical Li-ion storage capacity of the LYCB-CNF composite (Supplementary Fig. 1). Consequently, asymmetric CV curves are observed in both first and second cycles. This could be attributed to the formation of electronically conductive phases, which triggers the continuous reduction of LYCB separator from the LYCB-CNF–LYCB interface into the bulk. However, when the voltage window is limited to 0.2–2.5 V versus Li/Li^+, the cathodic and anodic peak currents become comparable, indicating reversible redox behaviour without the formation of electronically conductive products. This is further supported by discharge–charge profiles (Fig. 1b), showing initial capacities of 117 mAh g^{-1} for discharge and 83 mAh g^{-1} for charge. After subtracting the CNF contribution, LYCB delivers 84 mAh g^{-1} and 65 mAh g^{-1} for discharge and charge, corresponding to 1.43 mol and 1.11 mol Li^+ insertion and removal, respectively (Supplementary Note 1 and Supplementary Fig. 2). The partial irreversibility probably results from lithium loss due to reduced crystallinity (Supplementary Fig. 3) and surface reactions during the first cycle. In particular, LYCB shows negligible capacity decay over 20 cycles at 0.064 mA cm^{-2}, and maintains high stability with an average Coulombic efficiency (CE) of 100% at 0.64 mA cm^{-2} (Fig. 1c).

Since sulfide SEs are known to exhibit redox activity at low voltages, the discharge–charge behaviour of LPSC is evaluated for comparison under identical conditions (Supplementary Fig. 4). LPSC delivers an initial discharge capacity of 400 mAh g^{-1} but negligible charge capacity, attributed to the formation of ionically insulating decomposition products[20,21]. This is confirmed by EIS (Supplementary Fig. 5), showing a sharp increase in charge transfer resistance from 114.9 Ω (pristine) to 1,501.5 Ω (discharged), further rising to 3,755.4 Ω after charge, indicating poor redox reversibility of LPSC within 0.2–2.5 V versus Li/Li^+. By contrast, the Li-In|LYCB|LYCB-CNF cell shows reduced resistance and enhanced charge transfer after the first discharge (Supplementary Fig. 6), which remains low over 20 cycles, suggesting fundamentally different redox behaviour from LPSC.

Ex situ magic-angle spinning (MAS) ^{7}Li nuclear magnetic resonance (NMR) and X-ray diffraction (XRD) measurements are conducted to investigate LYCB's redox mechanism. Three distinct Li chemical environments are identified in the ^{7}Li NMR spectrum of pristine LYCB (Fig. 1d), assigned to different Li sites (Supplementary Table 1) in the monoclinic phase[22]. LYCB exclusively exhibits Li redistribution between these three crystallographic sites during electrochemical cycling, thereby confirming structural integrity at 0.2 V versus Li/Li^+ and evidencing reversible lithiation–delithiation behaviour. This is further confirmed by the XRD results (Fig. 1e), showing that the monoclinic $C2/m$ crystal structure is maintained throughout discharge–charge. The reversible shift of the (−131) and (131) reflections signifies a classic lithiation–delithiation solid-solution reaction (Fig. 1f). Figure 1g displays the evolution of the lattice parameters and cell volume obtained from Rietveld refinements (Supplementary Fig. 7 and Supplementary Tables 1–3). Lattice parameters and cell volume decrease on discharge, attributed to suppressed Coulombic repulsion between adjacent anion layers. On recharge, they increase but do not return to the pristine state, suggesting incomplete lithium recovery consistent with the initial capacity loss. Furthermore, XRD and scanning electron microscopy (SEM) measurements are performed on manually ground LYCB-CNF electrodes. Although this exposes much less interface for electrochemical reactions, as evidenced by a reduced capacity (Supplementary Fig. 8), it better represents LYCB's redox activity as a separator at the SE–electrode interface. The reversible peak shift on discharge–charge is also observed for manually ground

https://doi.org/10.1038/s41563-025-02296-6

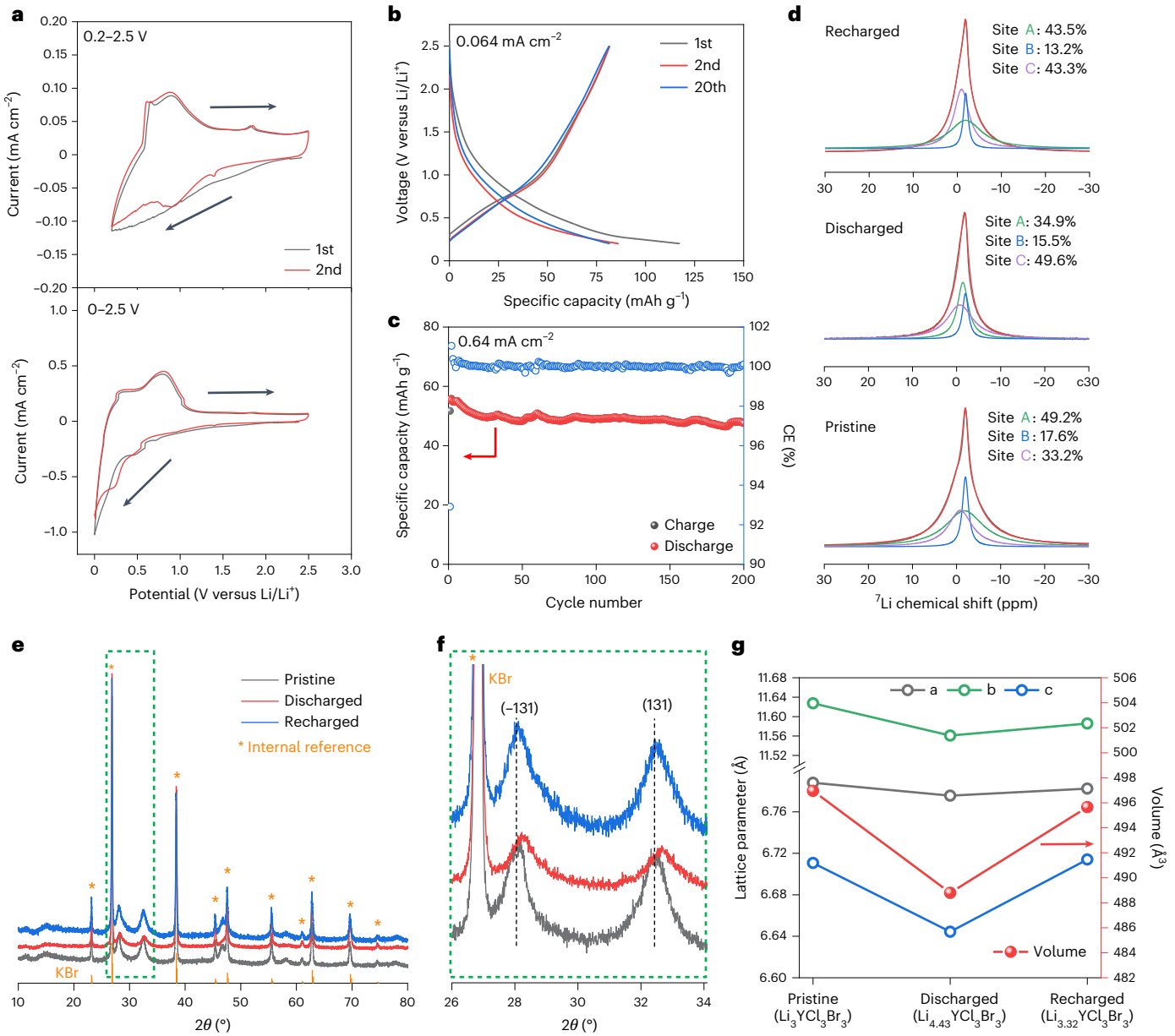

Fig. 1 | Electrochemical redox behaviour and structural characterization of LYCB. a, CV curves of the Li-In|LYCB|LYCB-CNF cell for voltage windows of 0–2.5 V versus Li/Li^+ and 0.2–2.5 V versus Li/Li^+ at 0.1 mV s^{-1}. The measurements are initiated with a negative scan. **b**, Voltage profiles of Li-In|LYCB|LYCB-CNF cell after the 1st, 2nd and 20th cycle under a current density of 0.064 mA cm^{-2}. **c**, Long-term cycling performance of the Li-In|LYCB|LYCB-CNF cell under 0.64 mA cm^{-2}. **d**, ^7Li MAS NMR spectra of LYCB at pristine, discharged and recharged states. On discharge, Li content at sites A and B decreases from 49.2% to 34.9% and from 17.6% to 15.5%, respectively, whereas at site C, it increases from 33.2% to 49.6%. Considering the actual Li stoichiometry, Li occupancy increases most substantially for sites B and C after discharge, attributed to the already high occupancy of site A in pristine LYCB (occupancies: site A, 0.74; site B, 0.26; site C, 0.25). **e**, Ex situ XRD patterns of LYCB-CNF from the Li-In|LYCB|LYCB-CNF cell at different states of charge. KBr is mixed with LYCB-CNF as an internal reference to clearly display the shift in XRD peaks due to LYCB (de)lithiation. **f**, Close-up view of the XRD patterns in **e**. The reduction in peak intensity reflects a decrease in crystallinity, whereas the increase in peak width can result from a combination of particle size reduction, amorphization and strain. Partial recovery of crystallinity on delithiation suggests that part of the loss in crystallinity is due to the strain in lithiated LYCB. **g**, Lattice parameters and unit-cell volume of the LYCB at different states of charge obtained from Rietveld refinement.

LYCB-CNF (Supplementary Fig. 9), where particle size reduction accompanied by partial amorphization appears to occur (Supplementary Fig. 10). Reversible lithiation–delithiation has also been observed for $Li_{1.5}Al_{0.5}Ti_{1.5}(PO_4)_3$ SE[14], occurring within its thermodynamically predicted stability window. In the case of LYCB, structurally similar to layered cathodes, the dynamic stability through lithiation–delithiation extends its practical stability limit down to 0.2 V versus Li/Li^+. In particular, the redox reaction through lithiation–delithiation requires electronic conductivity, typically low for SEs (2.8×10^{-9} S cm^{-1} for Li_3YCl_6 and 1.0×10^{-9} S cm^{-1} for Li_3YBr_6 (ref. 23)). It is suggested that the LYCB redox initially occurs only near the CNF, but the increased electronic conductivity on lithiation (Supplementary Fig. 11) enables bulk LYCB lithiation. This electronic conductivity increase does not cause short circuits, indicating that the redox activity remains confined to the anodic mixture and does not extend into the LYCB separator.

Additionally, DFT calculations are performed to deepen the understanding of LYCB's redox behaviour. In this analysis, the SE is treated as an electrode for Li insertion/extraction (reduction/oxidation), and

https://doi.org/10.1038/s41563-025-02296-6

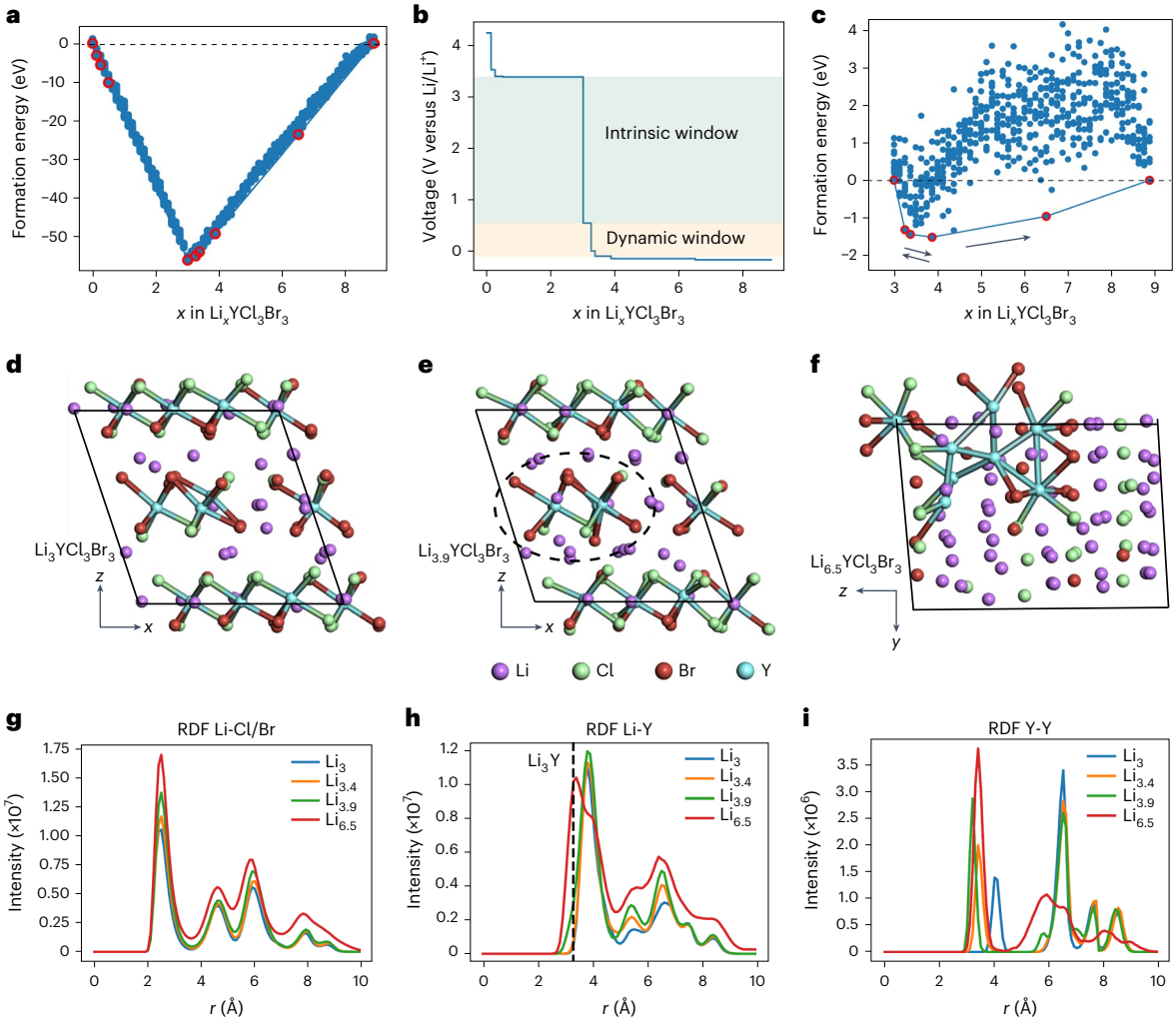

Fig. 2 | Stability window of LYCB as defined by DFT calculations. a, Formation enthalpies of $Li_xYCl_3Br_3$ with respect to the completely delithiated and lithiated states. The convex line follows the lowest-enthalpy path, indicating stable configurations along the range. **b**, Corresponding voltage profile indicating the intrinsic electrochemical window and dynamical region, where Li insertion (reduction is possible) occurs without destroying the structure framework. **c**, Formation enthalpies of $Li_xYCl_3Br_3$ with respect to LYCB and $Li_9YCl_3Br_3$. The reversible solid-solution region indicated with the back-and-forth arrows reaches the $Li_{3.9}YCl_3Br_3$ phase, followed by a first-order phase transition towards $Li_{6.5}YCl_3Br_3$. **d**–**f**, Configurational environment of LYCB (**d**), $Li_{3.9}YCl_3Br_3$ (**e**) and $Li_{6.5}YCl_3Br_3$ (**f**) phases after a 100-ps AIMD simulation at 400 K. **g**–**i**, RDFs for a 100-ps AIMD simulation at 400 K probing Li–Cl/Br (**g**), Li–Y (**h**) and Y–Y (**i**) distances.

its stability is assessed by constructing the convex hull and calculating the corresponding voltages. To ensure structural accuracy, multiple configurations are examined, including different Cl/Br orderings and Y occupations in the 4*a* and 4*h* Wyckoff positions (Methods). All cases yield consistent conclusions and the results for the structure defined by XRD refinement are presented here (Supplementary Fig. 12 and Supplementary Table 4).

The enthalpies of formation for $Li_xYCl_3Br_3$ (Fig. 2a) are referenced to fully delithiated ($Li_0YCl_3Br_3$) and fully lithiated ($Li_9YCl_3Br_3$) states, with the convex hull tracing the most stable compositions. The corresponding voltage profile (Fig. 2b) reveals an intrinsic electrochemical window between 3.4 V and 0.6 V versus Li/Li$^+$ and a dynamic lithiation region below 0.6 V versus Li/Li$^+$ (Supplementary Note 2). Although Li insertion is thermodynamically favourable near 0.6 V versus Li/Li$^+$, this does not necessarily lead to structural degradation. To investigate this, we focus on the low-voltage region (Fig. 2c), where the convex hull is replotted with reference to LYCB and $Li_9YCl_3Br_3$. Two distinct regions emerge: a solid-solution regime from LYCB to $Li_4YCl_3Br_3$, featuring homogeneous lithiation and a sloped voltage profile, and a first-order phase transition forming $Li_{6.5}YCl_3Br_3$ at higher Li concentrations. Ab initio molecular dynamics (AIMD) simulations are conducted on representative phases: LYCB, $Li_{3.4}YCl_3Br_3$, $Li_{3.9}YCl_3Br_3$ and $Li_{6.5}YCl_3Br_3$. Within the solid-solution regime, structural integrity is maintained after 100 ps (Fig. 2d,e), with the Y–Cl/Br octahedra preserved (Supplementary Note 3). Local distortion is limited to face-sharing octahedra, whose separations contract from 4.0/4.3 Å in LYCB to 3.2/3.4 Å in $Li_{3.9}YCl_3Br_3$, without compromising the layered framework. By contrast, $Li_{6.5}YCl_3Br_3$ undergoes structural collapse, with Y aggregation and the formation of Li–Cl/Br pairs (Fig. 2f).

Radial distribution function (RDF) plots (Fig. 2g–i) provide further structural insights. Li–Cl/Br RDFs remain similar across all phases, attributed to similar interatomic distances between LiCl/LiBr decomposition products and Li–Cl/Br distances in the LYCB lattice. However, Li–Y RDFs in $Li_{6.5}YCl_3Br_3$ show a new peak corresponding to the Li_3Y phase. In Y–Y RDFs, the 5–10-Å range shows consistent distances for solid-solution phases but a collapse in $Li_{6.5}YCl_3Br_3$ (Fig. 2i). In the 2–4-Å range, the first peak of LYCB shifts to lower distances in $Li_{3.4}YCl_3Br_3$ and $Li_{3.9}YCl_3Br_3$, reflecting converging face-sharing octahedra, differing from Y clustering in $Li_{6.5}YCl_3Br_3$ (Fig. 2f). These insights align with molecular dynamics (MD) simulation displacement plots (Supplementary Fig. 13). Also, $Li_{3.9}YCl_3Br_3$ and $Li_{3.4}YCl_3Br_3$ show faster mean square

https://doi.org/10.1038/s41563-025-02296-6

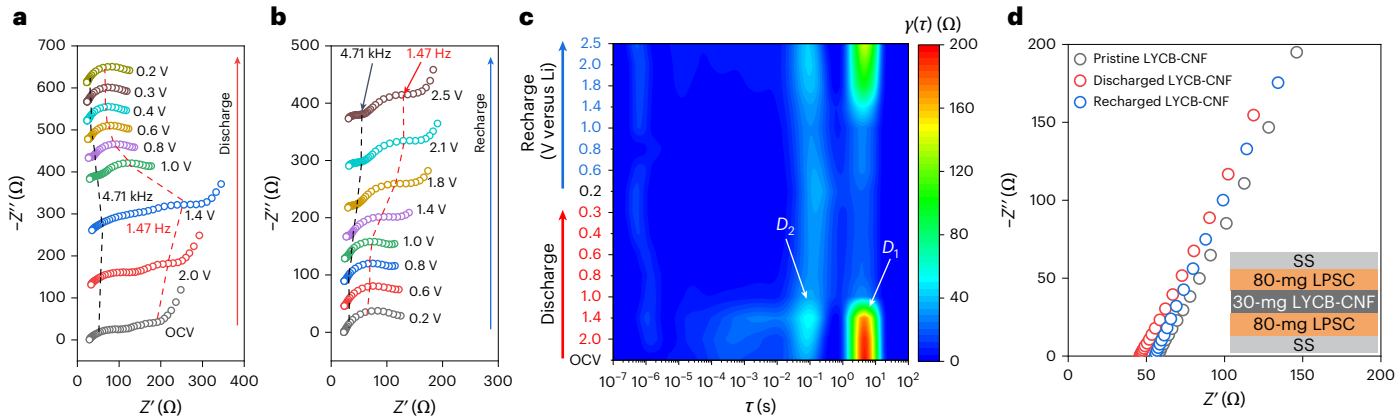

Fig. 3 | Evolution of Li-ion kinetics of LYCB during discharge–charge from EIS and corresponding DRT analyses. a, Nyquist plots of the Li-In|LYCB|LYCB-CNF cell at different discharge states. **b**, Nyquist plots of the Li-In|LYCB|LYCB-CNF cell at different recharge states. **c**, Two-dimensional intensity colour map of the DRT curves of the first discharge–charge process of the Li-In|LYCB|LYCB-CNF cell. OCV, open-circuit voltage. D_1 and D_2 have the highest time constant and resistance and are, thus, visible in the 2D intensity colour map. **d**, Nyquist plots of the SS-LPSC|LYCB-CNF|LPSC-SS symmetric cells. In these cells, 30 mg each of pristine, discharged or recharged LYCB-CNF composite powder is sandwiched between two LPSC layers (80 mg) to effectively block electron transport. Hence, the intersection point between the Nyquist plot and the *x* axis denotes the total ionic resistance of the two LPSC layers and the LYCB-CNF composite. The inset shows a schematic of the measurement setup.

displacement build-up than pristine LYCB, suggesting improved Li diffusivity in LYCB on lithiation.

The onset of Li insertion at 0.6 V versus Li/Li$^+$ matches well with the dynamic region observed experimentally (Fig. 1b) and the redox peak in Fig. 1a. Overall, reversible lithiation is supported in the LYCB–$Li_4YCl_3Br_3$ range, whereas higher lithiation levels ($Li_{6.5}YCl_3Br_3$) induce irreversible structural change. Compositions such as $Li_{4.43}YCl_3Br_3$ may lie on the boundary, potentially including both solid-solution and collapsed phases due to local overpotentials, leading to partial lithium trapping. Nevertheless, entropic contributions—by stabilizing near-hull phases—may slightly extend the reversible region beyond $Li_4YCl_3Br_3$, allowing LYCB to remain functional over a broader lithiation range (Supplementary Note 4 and Supplementary Fig. 14).

Evolution of Li-ion kinetics in LYCB on lithiation–delithiation

The redox activity, specifically the lithiation of LYCB at low potentials, is expected to impact its Li-ion conductivity. To investigate this, in situ EIS and related DRT analyses are used at different states of charge in Li-In|LYCB|LYCB-CNF cells. During discharge (Fig. 3a), two mid-frequency semicircles grow until 1.4 V versus Li/Li$^+$, potentially due to defects in ball-milled LYCB, though this remains speculative at this stage. Subsequently, the semicircles shrink and merge into one semicircle by 0.2 V versus Li/Li$^+$. Simultaneously, a shift in the characteristic frequency of the semicircles is observed, indicating that the redox state of LYCB substantially influences the charge transfer kinetics. Given the high stability of the Li-In–LYCB interface (Supplementary Fig. 15), the substantially reduced semicircles suggest enhanced interfacial charge transfer kinetics. On subsequent charge, the opposite trend is observed (Fig. 3b), consistent with the reversibility of the LYCB redox. The much smaller overall cell resistance at 0.2 V versus Li/Li$^+$, compared with the resistance at the open-circuit voltage, suggests a higher Li-ion conductivity for lithiated LYCB.

To better understand the evolution of Li-ion kinetics in LYCB, the DRT analysis (Supplementary Fig. 16 and Fig. 3c) of in situ EIS is performed to decouple the charge transport in the LYCB-CNF composite from the Li-In|LYCB and LYCB-CNF|LYCB interfaces[24,25]. The D_1 peak (1–10 s) corresponds to Li-ion transport in LYCB-CNF, whereas D_2 (~0.1 s) is attributed to charge transfer at the LYCB-CNF–LYCB interface[26]. Both D_1 and D_2 intensities decrease during discharge, indicating that LYCB lithiation improves both bulk conductivity and interfacial charge transfer. The slight increase in the D_2 time constant probably arises from contact loss due to volume changes in LYCB. On charging, the opposite trends are observed, confirming the reversibility of Li-ion kinetics and consistent with the reversible structural evolution of LYCB during redox processes.

The improved LYCB Li-ion conductivity on lithiation is directly demonstrated from the EIS measurements of stainless steel (SS)-LPSC|LYCB-CNF|LPSC-SS symmetric cells (Fig. 3d). The LYCB-CNF composite is sandwiched between two LPSC layers to prevent electronic conductivity contribution. In particular, the impact of possible chemical reaction between LPSC and LYCB is not expected here[27], as demonstrated by the stable resistance of the SS|LPSC|LYCB|SS cell after 3 days of resting (Supplementary Fig. 17). The overall resistances are 56.5 Ω, 45.3 Ω and 54.2 Ω for symmetric cells based on pristine, discharged and charged LYCB-CNF, respectively. After accounting for the LPSC resistance (Supplementary Fig. 18), the lithiated LYCB-CNF shows 3.2 times higher conductivity compared with pristine material.

Impact of LYCB redox activity on performance of RP anodes

RP has emerged as a promising next-generation anode candidate for liquid Li-ion batteries[28–30]. So far, however, only marginal progress has been reported on the utilization of RP in ASSBs, presenting unsatisfactory specific capacity, poor rate performance and limited cycle life[31,32], primarily due to poor electrochemical stability at the RP–SE interfaces and contact loss resulting from severe volume changes (over 300%) during lithiation[33]. Here, motivated by LYCB's dynamic stability down to 0.2 V versus Li/Li$^+$, three-dimensional RP-LYCB anodes with abundant chemically compatible RP–LYCB interfaces (Supplementary Fig. 19) are prepared by ball milling, which are evaluated in Li-In|LYCB|RP-LYCB half-cells. For comparison, RP-LPSC anodes are evaluated in Li-In|LPSC|RP-LPSC half-cells. The RP-LYCB anode demonstrates a discharge capacity of 2,641 mAh g^{-1} with a high initial CE of 87.51% (Fig. 4a), which rapidly surpasses 99% from the second cycle with minimal capacity decay. By contrast, RP-LPSC exhibits a lower initial CE (78.18%) and CE values below 91% over four subsequent cycles, with rapid capacity decline from 3,476 mAh g^{-1} to 2,490 mAh g^{-1} (Fig. 4b). Differential capacity curves confirm RP-LYCB's overlapping curves (Fig. 4c) versus decreasing peak intensities for RP-LPSC (Fig. 4d), proving that the RP anode is highly reversible in combination with

https://doi.org/10.1038/s41563-025-02296-6

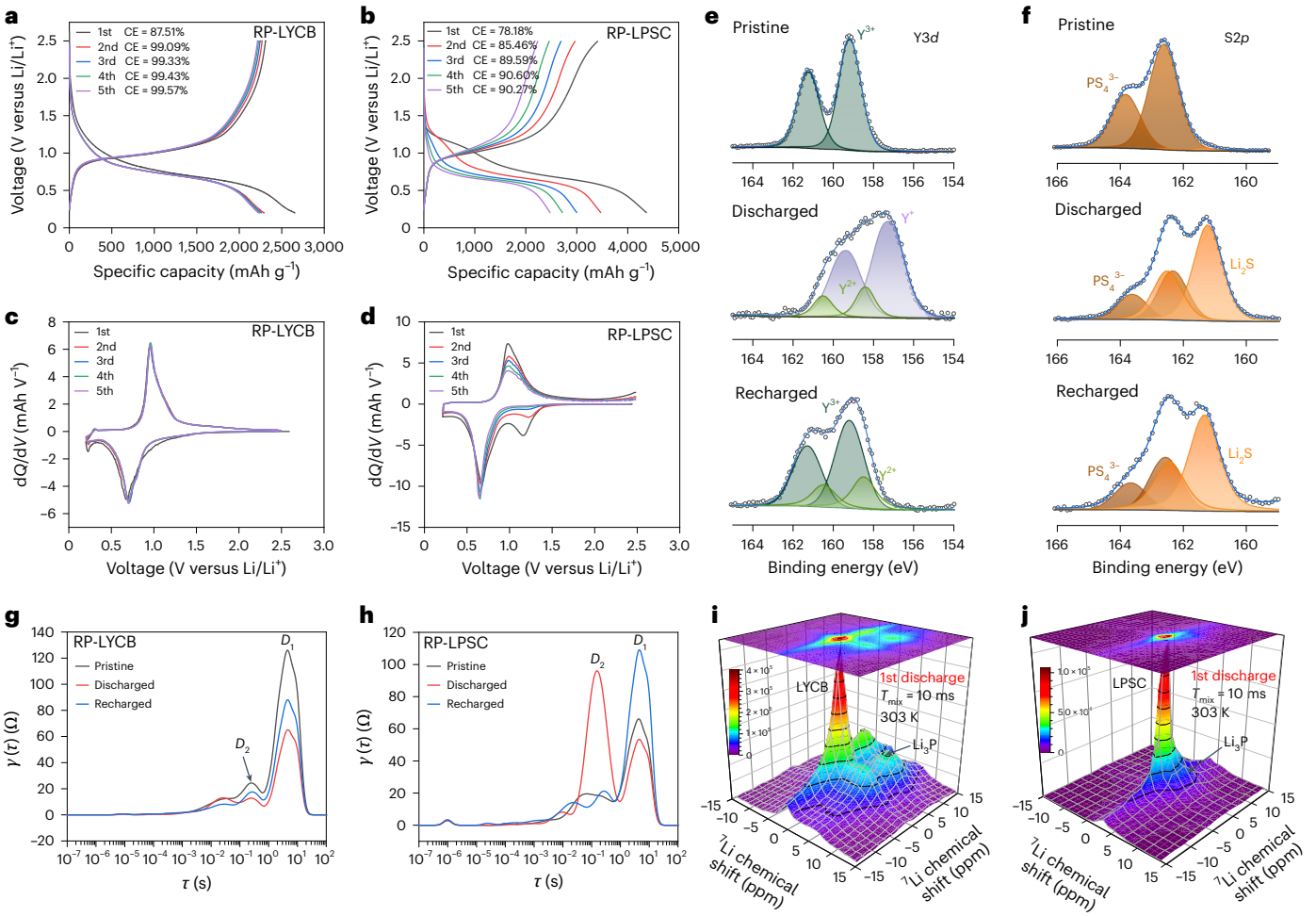

Fig. 4 | Electrochemical, EIS, XPS and NMR characterizations of LYCB- and LPSC-based RP anodes. a,**b**, Voltage profiles of the first five cycles for Li-In|LYCB|RP-LYCB (**a**) and Li-In|LPSC|RP-LPSC (**b**) cells. The RP mass loading is 0.6 mg cm^{-2} for both cells. **c**,**d**, Differential capacity profiles during the first five cycles for Li-In|LPSC|RP-LPSC (**c**) and Li-In|LPSC|RP-LPSC (**d**) cells. The RP mass loading is 0.6 mg cm^{-2} for both cells. **e**, Y3*d* XPS spectra of the RP-LYCB anode at the pristine, discharged and recharged states. **f**, S2*p* XPS spectra of the RP-LPSC anode at the pristine, discharged and recharged states. **g**, DRT curves from the EIS measurements of the Li-In|LYCB|RP-LYCB cell at the pristine, discharged and recharged states. **h**, DRT curves of the Li-In|LPSC|RP-LPSC cell curves from EIS measurements at pristine, discharged and recharged states. **i**, ^{7}Li NMR 2D exchange spectrum of the RP-LYCB anode after the first discharge at 303 K measured with a mixing time of 10 ms. **j**, ^{7}Li 2D NMR exchange spectrum of the RP-LPSC anode after the first discharge at 303 K measured with a mixing time of 10 ms.

LYCB, whereas it severely degrades with LPSC. Although both RP-LYCB and RP-LPSC anodes exhibit reversible P/Li_3P redox (Supplementary Figs. 20 and 21), Y3*d* (Fig. 4e) and S2*p* (Fig. 4f) XPS data reveal stark reversibility disparities between RP-LYCB and RP-LPSC. Y^{3+} (159.2 eV) in the pristine RP-LYCB is reduced to Y^{+} (157.3 eV) and Y^{2+} (158.3 eV) after discharge, which oxidizes back to Y^{2+} and Y^{3+} after subsequent recharge. By contrast, RP-LPSC forms irreversible Li_2S, corroborated by residual Li_2S in ^{7}Li NMR and XRD results of the recharged RP-LPSC anode (Supplementary Figs. 21 and 22).

EIS (Supplementary Figs. 23 and 24) coupled with DRT analyses (Fig. 4g,h) reveal different Li-ion kinetics between RP-LYCB and RP-LPSC systems. For RP-LYCB, interfacial (D_2) and charge transport (D_1) resistances substantially decrease on discharge (Fig. 4g) due to enhanced LYCB ionic conductivity and the formation of ionic conductive Li_3P (0.57 mS cm^{-1})[34]. These resistances increase back during charging but remain lower compared with the pristine state, reflecting the reversible LYCB delithiation and the Li_3P/P phase transition. By contrast, in RP-LPSC, although Li_3P formation temporarily improves conductivity (D_1 reduction in Fig. 4h), irreversible LPSC decomposition leads to persistent interface degradation. This is evidenced by the elevated D_2 for discharged RP-LPSC, increased D_1 for recharged RP-LPSC and the emerging large semicircle in the EIS for discharged RP-LPSC (Supplementary Fig. 24), all indicative of charge transport barriers from residual Li_2S.

To gain an insight into the local Li-ion transport across the RP–SE interfaces, we use two-dimensional (2D) NMR exchange experiments, which non-invasively quantify spontaneous Li-ion diffusion across solid–solid interfaces[35,36]. In the 2D exchange spectrum of discharged RP-LYCB (Fig. 4i), distinct off-diagonal cross-peaks appear at 10-ms mixing time and 303 K, indicating substantial Li-ion exchange between Li_3P and lithiated LYCB. This efficient exchange persists after 25 cycles (Supplementary Fig. 25). By contrast, no cross-peaks are observed for discharged RP-LPSC (Fig. 4j), suggesting undetectable Li-ion flux and poor interface kinetics. By fitting the evolution of the cross-peak intensity as a function of mixing time to a diffusion model derived from Fick's law[37,38] (Supplementary Note 5), the activation energies of 0.241 eV (1st discharge; Supplementary Fig. 26) and 0.251 eV (25th discharge; Supplementary Fig. 27) are obtained for RP-LYCB, confirming stable and efficient Li-ion transport across the RP–LYCB interface during cycling.

https://doi.org/10.1038/s41563-025-02296-6

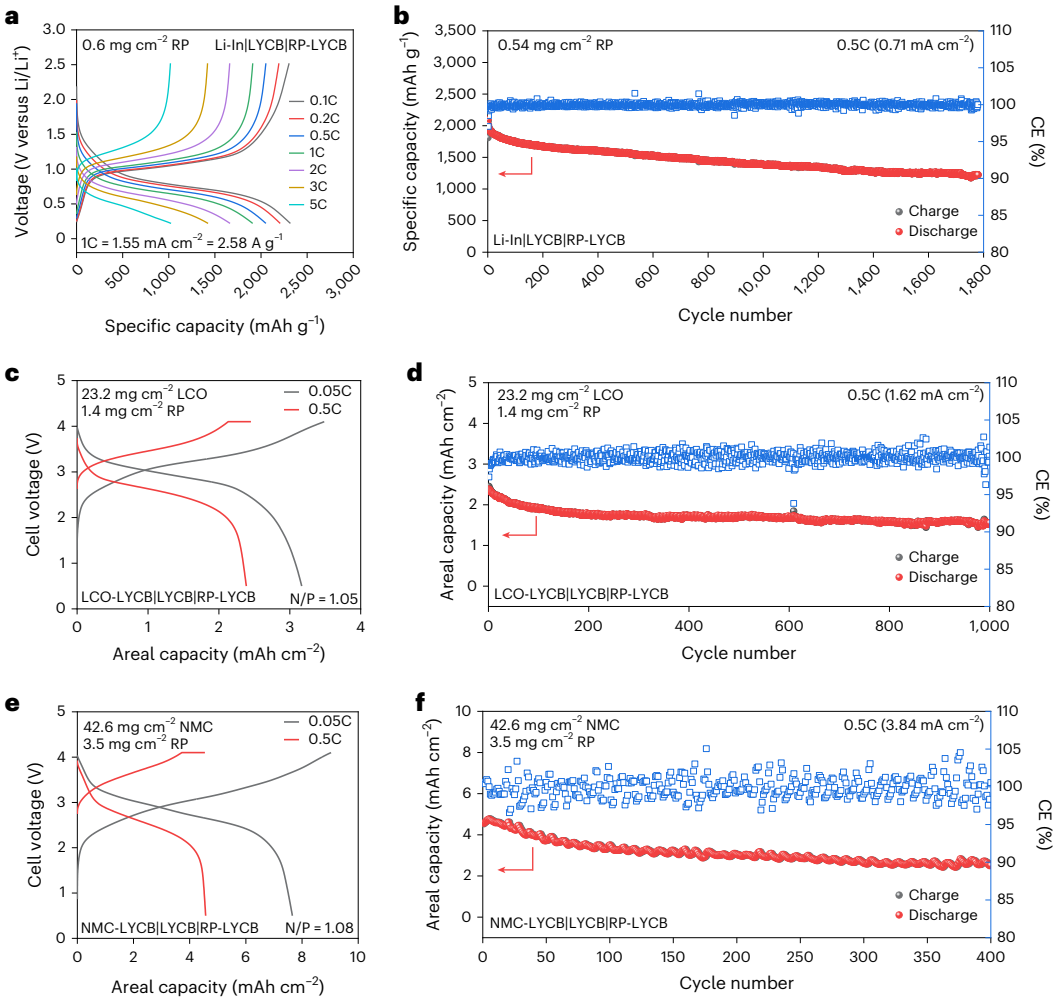

Fig. 5 | Electrochemical performance of Li-In|LYCB|RP-LYCB half-cell and LCO-LYCB and NMC-LYCB|LYCB|RP-LYCB full cells. a, Galvanostatic discharge–charge voltage profiles of the Li-In|LYCB|RP-LYCB half-cell at different rates. **b**, Cycling stability and CE of the Li-In|LYCB|RP-LYCB half-cell at 0.5C. **c**, Galvanostatic discharge–charge voltage profiles of the uncoated LCO-LYCB|LYCB|RP-LYCB full cell at 0.05C and 0.5C. **d**, Cycling stability and CE of uncoated LCO-LYCB|LYCB|RP-LYCB full cell at 0.5C. **e**, Galvanostatic discharge–charge voltage profiles of the uncoated NMC-LYCB|LYCB|RP-LYCB full cell at 0.05C and 0.5C. **f**, Cycling stability and CE of an uncoated NMC-LYCB|LYCB|RP-LYCB full cell at 0.5C. All the electrochemical tests are conducted at room temperature.

Electrochemical characterization of half- and full cells

Benefiting from the efficient Li-ion transport at the RP–LYCB interface, Li-In|LYCB|RP-LYCB half-cells exhibit excellent rate capability at room temperature (Fig. 5a and Supplementary Fig. 28a). At a high rate of 5C (7.75 mA cm^{-2}), the cell delivers 1,024 mAh g^{-1}, 44% of the capacity at 0.1C (Supplementary Fig. 28b). EIS and DRT results (Supplementary Fig. 29) confirm that high Li-ion diffusivity at the RP–SE interface and within the RP-LYCB is sustained over 300 cycles. Consequently, the cell achieves 1,780 stable cycles at 0.5C with 61% capacity retention (Fig. 5b). By contrast, the Li-In|LPSC|RP-LPSC half-cell shows rapid capacity fading and poor rate performance (876 mAh g^{-1} at 0.5C; Supplementary Fig. 30).

Leveraging LYCB's redox activity at low potentials and its high-voltage stability, high-performance full cells based on a single LYCB SE are demonstrated, with RP as the anode and uncoated LCO or NMC as the cathode. The LCO-LYCB|LYCB|RP-LYCB cell with 23.2 mg cm^{-2} LCO and an N/P (negative/positive) electrode capacity ratio of 1.05 delivers 3.2 mAh cm^{-2} at 0.05C (Fig. 5c) and retains 70% capacity after 1,000 cycles at 0.5C (Fig. 5d). At 38 mg cm^{-2} LCO loading, 4.4 mAh cm^{-2} and 100 stable cycles are achieved (Supplementary Fig. 31). For the NMC-LYCB|LYCB|RP-LYCB full cell (42.6 mg cm^{-2}, N/P = 1.08), an areal capacity of 7.68 mAh cm^{-2} (180 mAh g^{-1}) is delivered at 0.05C, with 63% retention after 400 cycles at 0.5C (Fig. 5e,f). In particular, consistent capacity fade in both half- and full cells is attributed to RP volume changes during cycling and capacity curve oscillations are due to day–night fluctuations of room temperature.

The generality of dynamic stability in SEs is further demonstrated in the more cost-effective halide LZC SE having the trigonal structure (Supplementary Fig. 32), showing a reversible redox activity at voltages lower than its reported reduction stability limit (2 V versus Li/Li$^+$)[39,40]. As observed in Supplementary Fig. 33, the LZC SE shows a reversible specific capacity of 45 mAh g^{-1} (0.55-mol Li$^+$) and stable cycling down to 1.4 V versus Li/Li$^+$, which is achieved through structurally reversible lithiation–delithiation, supported by ex situ XRD results and corresponding Rietveld refinements (Supplementary Fig. 34 and Supplementary Tables 5–7). Similar to LYCB, LZC shows enhanced Li-ion kinetics after lithiation (Supplementary Fig. 35). This redox activity offers LZC dynamic stability down to 1.4 V versus Li/Li$^+$, enabling the use of $Li_4Ti_5O_{12}$ (LTO) as an anode. The LTO-LZC anode delivers a capacity of 237 mAh g^{-1}, with 19% stemming from LZC's reversible redox reaction (Supplementary Fig. 36). Moreover, it demonstrates long-term cycling stability (250 cycles) and high-areal-capacity capability (2 mAh cm^{-2}).

https://doi.org/10.1038/s41563-025-02296-6

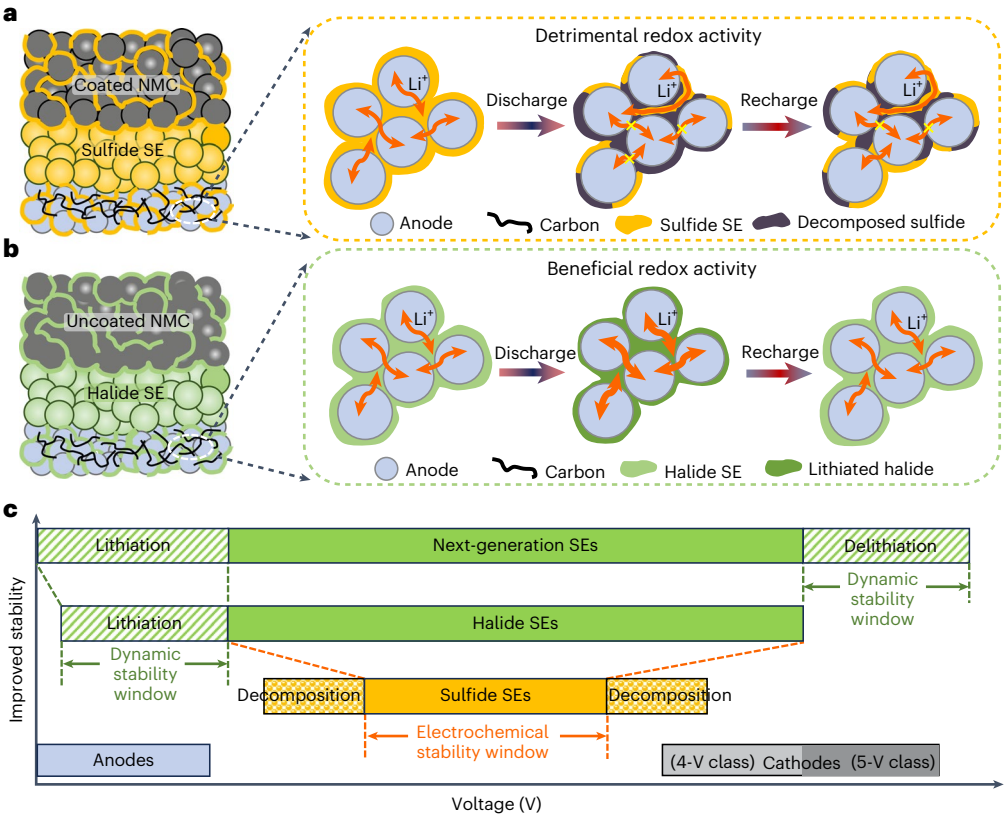

Fig. 6 | Schematic of redox activity and stability window of sulfide and halide SEs and design perspective for future SEs. a, In sulfide-SE-based ASSBs, reduction beyond the electrochemical stability window results in insulating decomposition products that severely impede Li-ion transport between the anode and SE. Although reduced sulfide decomposition products can be partially reoxidized, in combination with other decomposition products, this introduces a large barrier for Li-ion transport at the anode–SE interface. In addition, the poor oxidation stability of sulfides makes them incompatible with high-voltage NMC cathodes, necessitating, for instance, a protective coating on the cathode particles. **b**, In the halide SEs studied at present, reduction of halide SEs leads to the formation of a lithiated phase instead of decomposition products at potentials that are beyond the formal stability limit. Lithiated halide has improved ionic conductivity. Hence, rather than compromising Li-ion transport at the anode–SE interface, it enhances transport kinetics, as indicated by the thicker Li-ion transport arrows. The intrinsic high-voltage stability of halide SEs enables the use of uncoated NMC cathodes in the full cells. **c**, Various stability windows of SEs and the present concept, where the reversible SE redox activity is utilized to develop next-generation ASSBs with active SEs. Within the electrochemical stability window, the SE obviously does not show any redox activity. When exposed to potentials outside this window, sulfide SEs decompose at both high and low potentials, whereas halide SEs allow reversible lithiation–delithiation at low potentials. The voltage range in which reversible lithiation–delithiation occurs is defined as the dynamic stability window. On the basis of this, the current proposition is that the next-generation SEs with a wider dynamic stability window can lead to ASSBs that are more stable and provide additional capacity.

Discussion

To establish high-performance anode–SE interfaces, electrochemically stable SEs are typically preferred. However, current highly conductive SEs, such as sulfides and halides, are electrochemically unstable at the low potentials required for most anodes. As illustrated in Fig. 6a, sulfide SEs decompose into ionically insulating products such as Li_2S and LiCl, thereby increasing the interfacial resistance. This decomposition renders sulfide SEs incompatible with low-potential anodes, although kinetically stabilized SE interphases can be achieved through specific anode–sulfide SE combinations. Similarly, sulfides face comparable challenges at the cathode interface, where operation beyond the stability window necessitates protective cathode coatings, introducing an additional step and challenge.

By contrast, halide SEs such as LYCB and LZC exhibit fundamentally different redox behaviour on reduction. Rather than decomposing, they retain their crystal structure and undergo reversible lithiation/delithiation at low potentials (Fig. 6b). This reversibility yields three advantages, including an expanded practical stability window (from 0.62 V to 0.2 V versus Li/Li^+ for LYCB and from 2 V to 1.4 V versus Li/Li^+ for LZC), improved ionic conductivity at the electrode interface that promotes high rate performance, and additional capacity that is particularly valuable for low-capacity anodes like LTO. Combined with their high-voltage stability, halides like LYCB enable high-performance full cells using a single-halide SE, uncoated cathodes and low-potential anodes, offering a more cost-effective ASSB solution over other rare-earth halides.

The stability window of SEs is usually determined as the voltage range in which no reduction/oxidation occurs. This applies to sulfides, where reactions beyond the thermodynamic window cause irreversible decomposition into known stable phases (Fig. 6c). Some SEs, such as $Li_{1.5}Al_{0.5}Ti_{1.5}(PO_4)_3$, have demonstrated reversible redox behaviour within their thermodynamic limits, but this does not expand their practical voltage range. By contrast, halide SEs (for example, LYCB and LZC) retain structural integrity beyond their predicted stability window, introducing a dynamic stability window. The monoclinic structure of LYCB resembles that of NMC cathodes, supporting its active redox role and maintaining structural integrity. Additionally, the lithiation-induced reduction of Y^{3+} to Y^{2+}/Y^{+} may enhance electronic conductivity, promoting redox utilization in the anodic mixture. However, this activity must be confined, as deeper reduction (for example, to metallic Y) may trigger irreversible degradation. In particular, cycling LYCB to 0.2 V versus Li/Li^+ remains reversible, but further study is needed to clarify the role of electronic conductivity.

The present results motivate further detailed investigations into the reversible redox activity of SEs, starting with other halide compounds. Further research will reveal whether this behaviour can be extended to enable Li-metal and Si anodes, and if it can be leveraged at the cathode—potentially enabling applications with 5-V cathodes (Fig. 6c) to further boost the energy density. The dynamic stability window, where the SE functions as an electrode in the vicinity of the electrode, deepens our understanding of the SE's role and expands the possibilities in designing high-performance electrode–SE interfaces in ASSBs.

Online content

Any methods, additional references, Nature Portfolio reporting summaries, source data, extended data, supplementary information, acknowledgements, peer review information; details of author contributions and competing interests; and statements of data and code availability are available at https://doi.org/10.1038/s41563-025-02296-6.

References

1. Manthiram, A., Yu, X. & Wang, S. Lithium battery chemistries enabled by solid-state electrolytes. *Nat. Rev. Mater.* **2**, 16103 (2017).
2. Famprikis, T., Canepa, P., Dawson, J. A., Islam, M. S. & Masquelier, C. Fundamentals of inorganic solid-state electrolytes for batteries. *Nat. Mater.* **18**, 1278–1291 (2019).
3. Wang, C. et al. All-solid-state lithium batteries enabled by sulfide electrolytes: from fundamental research to practical engineering design. *Energy Environ. Sci.* **14**, 2577–2619 (2021).
4. Richards, W. D., Miara, L. J., Wang, Y., Kim, J. C. & Ceder, G. Interface stability in solid-state batteries. *Chem. Mater.* **28**, 266–273 (2016).
5. Zhu, Y., He, X. & Mo, Y. Origin of outstanding stability in the lithium solid electrolyte materials: insights from thermodynamic analyses based on first-principles calculations. *ACS Appl. Mater. Interfaces* **7**, 23685–23693 (2015).
6. Park, K. H. et al. Design strategies, practical considerations, and new solution processes of sulfide solid electrolytes for all-solid-state batteries. *Adv. Energy Mater.* **8**, 1800035 (2018).
7. Wang, C., Liang, J., Kim, J. T. & Sun, X. Prospects of halide-based all-solid-state batteries: from material design to practical application. *Sci. Adv.* **8**, eadc9516 (2022).
8. Tanaka, Y. et al. New oxyhalide solid electrolytes with high lithium ionic conductivity >10 mS cm^{-1} for all-solid-state batteries. *Angew. Chem. Int. Ed.* **62**, e202217581 (2023).
9. Riegger, L. M., Schlem, R., Sann, J., Zeier, W. G. & Janek, J. Lithium-metal anode instability of the superionic halide solid electrolytes and the implications for solid-state batteries. *Angew. Chem.* **133**, 6792–6797 (2021).
10. Rosenbach, C. et al. Visualizing the chemical incompatibility of halide and sulfide-based electrolytes in solid-state batteries. *Adv. Energy Mater.* **13**, 2203673 (2023).
11. Koç, T. et al. Toward optimization of the chemical/electrochemical compatibility of halide solid electrolytes in all-solid-state batteries. *ACS Energy Lett.* **7**, 2979–2987 (2022).
12. Auvergniot, J. et al. Interface stability of argyrodite Li_6PS_5Cl toward $LiCoO_2$, $LiNi_{1/3}Co_{1/3}Mn_{1/3}O_2$, and $LiMn_2O_4$ in bulk all-solid-state batteries. *Chem. Mater.* **29**, 3883–3890 (2017).
13. Han, F., Zhu, Y., He, X., Mo, Y. & Wang, C. Electrochemical stability of $Li_{10}GeP_2S_{12}$ and $Li_7La_3Zr_2O_{12}$ solid electrolytes. *Adv. Energy Mater.* **6**, 1501590 (2016).
14. Schwietert, T. K., Vasileiadis, A. & Wagemaker, M. First-principles prediction of the electrochemical stability and reaction mechanisms of solid-state electrolytes. *JACS Au* **1**, 1488–1496 (2021).
15. Schwietert, T. K. et al. Clarifying the relationship between redox activity and electrochemical stability in solid electrolytes. *Nat. Mater.* **19**, 428–435 (2020).
16. Tan, D. H. S. et al. Elucidating reversible electrochemical redox of Li_6PS_5Cl solid electrolyte. *ACS Energy Lett.* **4**, 2418–2427 (2019).
17. Arbi, K., Kuhn, A., Sanz, J. & García-Alvarado, F. Characterization of lithium insertion into NASICON-type $Li_{1+x}Ti_{2-x}Al_x(PO_4)_3$ and its electrochemical behavior. *J. Electrochem. Soc.* **157**, A654 (2010).
18. Wang, Q. et al. Designing lithium halide solid electrolytes. *Nat. Commun.* **15**, 1050 (2024).
19. Li, X. et al. Structural regulation of halide superionic conductors for all-solid-state lithium batteries. *Nat. Commun.* **15**, 53 (2024).
20. Ohno, S., Rosenbach, C., Dewald, G. F., Janek, J. & Zeier, W. G. Linking solid electrolyte degradation to charge carrier transport in the thiophosphate-based composite cathode toward solid-state lithium-sulfur batteries. *Adv. Funct. Mater.* **31**, 2010620 (2021).
21. Ohno, S. et al. Observation of chemomechanical failure and the influence of cutoff potentials in all-solid-state Li–S batteries. *Chem. Mater.* **31**, 2930–2940 (2019).
22. Liu, Z. et al. High ionic conductivity achieved in $Li_3Y(Br_3Cl_3)$ mixed halide solid electrolyte via promoted diffusion pathways and enhanced grain boundary. *ACS Energy Lett.* **6**, 298–304 (2021).
23. Asano, T. et al. Solid halide electrolytes with high lithium-ion conductivity for application in 4 V class bulk-type all-solid-state batteries. *Adv. Mater.* **30**, 1803075 (2018).
24. Sun, S. et al. Eliminating interfacial O-involving degradation in Li-rich Mn-based cathodes for all-solid-state lithium batteries. *Sci. Adv.* **8**, eadd5189 (2022).
25. Lu, Y., Zhao, C.-Z., Huang, J.-Q. & Zhang, Q. The timescale identification decoupling complicated kinetic processes in lithium batteries. *Joule* **6**, 1172–1198 (2022).
26. Lu, P. et al. Wide-temperature, long-cycling, and high-loading pyrite all-solid-state batteries enabled by argyrodite thioarsenate superionic conductor. *Adv. Funct. Mater.* **33**, 2211211 (2023).
27. Samanta, S. et al. Ionocovalency of the central metal halide bond-dependent chemical compatibility of halide solid electrolytes with Li_6PS_5Cl. *ACS Energy Lett.* **9**, 3683–3693 (2024).
28. Jin, H., Huang, Y., Wang, C. & Ji, H. Phosphorus-based anodes for fast charging lithium-ion batteries: challenges and opportunities. *Small Sci.* **2**, 2200015 (2022).
29. Sun, Y. et al. Design of red phosphorus nanostructured electrode for fast-charging lithium-ion batteries with high energy density. *Joule* **3**, 1080–1093 (2019).
30. Cheng, Z., Wu, Y. & Huang, H. Red phosphorus/graphite composite as a high performance anode for lithium-ion batteries. *Solid State Ion.* **389**, 116098 (2023).
31. Nagao, M., Hayashi, A. & Tatsumisago, M. All-solid-state lithium secondary batteries with high capacity using black phosphorus negative electrode. *J. Power Sources* **196**, 6902–6905 (2011).
32. Yang, J. et al. Building a C-P bond to unlock the reversible and fast lithium storage performance of black phosphorus in all-solid-state lithium-ion batteries. *Mater. Today Energy* **20**, 100662 (2021).
33. Han, X., Gong, H., Li, H. & Sun, J. Fast-charging phosphorus-based anodes: promises, challenges, and pathways for improvement. *Chem. Rev.* **124**, 6903–6951 (2024).
34. Li, J. et al. Mixed ion-electron conducting Li_3P for efficient cathode prelithiation of all-solid-state Li-ion batteries. *SmartMat* **4**, e1200 (2023).
35. Liu, M. et al. Improving Li-ion interfacial transport in hybrid solid electrolytes. *Nat. Nanotechnol.* **17**, 959–967 (2022).
36. Cheng, Z. et al. Revealing the impact of space-charge layers on the Li-ion transport in all-solid-state batteries. *Joule* **4**, 1311–1323 (2020).

37. Wagemaker, M., Kentgens, A. P. M. & Mulder, F. M. Equilibrium lithium transport between nanocrystalline phases in intercalated TiO_2 anatase. *Nature* **418**, 397–399 (2002).
38. Ganapathy, S., Yu, C., van Eck, E. R. H. & Wagemaker, M. Peeking across grain boundaries in a solid-state ionic conductor. *ACS Energy Lett.* **4**, 1092–1097 (2019).
39. Ganesan, P. et al. Fluorine-substituted halide solid electrolytes with enhanced stability toward the lithium metal. *ACS Appl. Mater. Interfaces* **15**, 38391–38402 (2023).
40. Wang, K. et al. A cost-effective and humidity-tolerant chloride solid electrolyte for lithium batteries. *Nat. Commun.* **12**, 4410 (2021).

Methods

Synthesis

LYCB was synthesized as described in detail previously[41]. Appropriate amounts of LiBr (99.9%, Alfa Aesar) and YCl_3 (99.9%, Sigma-Aldrich) were pelletized and sealed in quartz tubes. The pellet was annealed at 650 °C for 48 h and then naturally cooled down to room temperature, which was finally manually ground with a mortar and pestle to obtain LYCB powder. LPSC (3–5 μm; NEI Corporation) was used as received without further treatment. For the preparation of LZC, a stoichiometric mixture of LiCl (99.99%, Sigma-Aldrich) and $ZrCl_4$ (99.99%, Sigma-Aldrich) was ball milled at 550 rpm for 10 h in a ZrO_2-coated SS jar with 10-mm ZrO_2 balls using Pulverisette 7PL (Fritsch).

Solid-state battery assembly and electrochemical cycling

LYCB-CNF, LPSC-CNF and LZC-CNF composites were prepared by ball milling the LYCB (LPSC and LZC) and CNF (Sigma-Aldrich) or Super C at a mass ratio of 5:1 at 400 rpm for 2 h. The manually ground LYCB-CNF composite was prepared by manually mixing LYCB and CNF at a mass ratio of 5:1 using a mortar and pestle for 10 min. For the Li-In|LYCB|LYCB-CNF (Super C) and Li-In|LPSC|LPSC-CNF cells, 80 mg of LYCB (LPSC) was first pressed in a solid-state cell at 65 MPa for 1 min and then 10 mg of LYCB (LPSC)-CNF (Super C) composite was spread on top of LYCB (LPSC) and pressed at 320 MPa for 3 min. Note that the LYCB and LPSC densified after 3 min of 320-MPa pressure show similar porosities, as evidenced by the SEM images in Supplementary Fig. 37. Li-In alloy composed of 2-mg Li and 45-mg In was placed on the another side of LYCB (LPSC) and the cell was pressed at 65 MPa for 3 min. The Li-In|LYCB|LYCB-CNF and Li-In|LPSC|LPSC-CNF cells were cycled in a voltage window of 0.2–2.5 V versus Li/Li^+. Li-In|LPSC-LZC|LZC-CNF cells were assembled in a similar way, except for introducing an extra LPSC layer of 30 mg between the LZC and Li-In alloy (avoiding the side reaction between LZC and Li-In alloy) and cycling in a voltage window of 1.4–3 V versus Li/Li^+. For the RP-LYCB and RP-LPSC composites, RP and Ketjenblack (EC-600JD) were pelletized at a mass ratio of 7:3 and sealed in a quartz tube, which was annealed at 600 °C at a heating rate of 10 °C min^{-1} for 2 h and subsequently cooled down to 280 °C at a rate of 1 °C min^{-1} for 10 h. Then, RP@Ketjenblack was ball milled with LYCB (LPSC) and CNF at a mass ratio of 2:3:1 at 400 rpm for 4 h. The Li-In|LYCB|RP-LYCB cells and Li-In|LPSC|RP-LPSC cells were assembled with similar processes for Li-In|LYCB|LYCB-CNF cells, except for replacing the LYCB-CNF composite with the RP-LYCB or RP-LPSC composite, respectively. For the Li-In|LPSC-LZC|LTO-LZC cells, LTO, LZC and CNF were ball milled with a weight ratio of 4:5:1 at 400 rpm for 2 h to get the LTO-LZC composite. Then, LTO-LZC was spread on the LZC surface of the LPSC-LZC bilayer SE (LPSC serves as a protective layer at the anode side), whereas the Li-In alloy was added on the other side. The cell was pressed at 65 MPa for 3 min and cycled in 1.4–3 V versus Li/Li^+. For the full cells, uncoated LCO or NMC (MSE Supplies) was manually ground with LYCB in a mortar at a weight ratio of 7:3 for 10 min. Later, 80 mg of LYCB was pressed in the solid-state cell at 65 MPa for 1 min and then the LCO-LYCB or NMC-LYCB composite was spread on one side of LYCB, whereas the RP-LYCB composite was spread on the other side of LYCB. The full cell was pressed at 320 MPa for 3 min. All the cell assembly processes were performed in an argon-filled glovebox. The SS-LPSC|LYCB|LPSC-SS symmetric cell was assembled by sandwiching 30 mg of LYCB-CNF between two LPSC layers (80 mg each) in the solid-state cell. All the electrochemical cycling tests were conducted under a stacking pressure of 65 MPa and at room temperature using a LANHE battery test system (CT2001A). The CV and EIS measurements were performed using a VMP3 multichannel potentiostat (BioLogic EC-Lab). The perturbation voltage of 5 mV in the frequency range of 7 MHz to 0.1 Hz was applied for EIS measurements. The DRT analysis was conducted based on the EIS results with RelaxIS 3 software.

Characterization

XRD patterns were collected on an X'Pert Pro X-ray diffractometer (PANalytical) in the 2θ range of 10–80° using Cu Kα X-rays (1.5406 Å at 45 kV and 40 mA). The samples were tested in an airtight sample holder, filled with argon, to prevent exposure to oxygen and moisture. Rietveld refinements were conducted on LYCB and LZC at different states of discharge–charge with GSAS-II (ref. 42) to obtain the lattice parameters. Only instrument parameters, background, lattice parameters, size and strains were carefully refined. The morphologies were analysed by an SEM instrument (HITACHI S4800). An X-ray photoelectron spectrometer was used to investigate the chemical state in the samples (Thermo Fisher K-Alpha spectrometer). The samples were placed in an airtight sample holder and transferred to the XPS spectrometer under vacuum to prevent moisture/air exposure. The XPS spectrometer has a focused monochromatic Al Kα source (1,486.6 eV) anode operating at 36 W (12 kV, 3 mA), a flood gun operating at 1 V and 100 μA, and the base pressure inside the analysis chamber was approximately 2×10^{-9} mbar. The spot size used was approximately $800 \times 400\ \mu m^2$ and the pass energy of the analyser was set to 50 eV. Measurements were performed at least on three points on each sample, providing highly similar results. In the analysis, the C–C peak at 284.8 eV was taken as a reference for the charge shift. The peaks were fitted using 70% Gaussian and 30% Lorentzian line shapes (weighted least squares fitting method) and nonlinear Shirley-type background using the Thermo Fisher Avantage software (Version 5.986). Solid-state NMR measurements were performed on a Bruker Ascend 500 magnet ($B_0 = 11.7$ T) with a NEO console operating at a ^7Li resonance frequency of 194.317 MHz. Single-pulse ^7Li MAS NMR spectra were recorded for samples packed in 3.2-mm rotor. A 90° radio-frequency pulse lasting approximately 4 μs was applied, and a recycle delay of 1 s was used to ensure quantitative measurement conditions. Variable-temperature 2D exchange measurements were performed using a 4-mm MAS probe from 303 K to 343 K at a spinning speed of 10 kHz.

Ab initio calculations

The DFT calculations utilized the Perdew–Burke–Ernzerhof generalized gradient approximation with the PBEsol functional within the Vienna ab initio simulation package[43–45]. Initially, structure relaxation used a cut-off energy of 400 eV and a $3 \times 3 \times 3$ k-point mesh, subsequently reduced to 300 eV and $1 \times 1 \times 1$ k points for MD simulations. MD simulations were conducted in the NVT ensemble with a time step of 2 fs, totalling 100 ps. All the calculations were spin polarized and performed in $2 \times 1 \times 2$ supercells ($13.47 \times 12.04 \times 13.6$ Å^3). To determine the intrinsic electrochemical window, convex hulls, capturing the formation enthalpies during Li extraction/insertion (oxidation/reduction), were constructed, computationally treating the electrolyte as a typical electrode. The principles for these charge-neutral SE calculations were established in refs. 14,15. Accordingly, the formulations in this work for the reaction and voltage calculations are

$$Li_3YCl_3Br_3 \rightarrow Li_xYCl_3Br_3 + (3-x)\,Li.$$

If $x < 3$, LYCB is oxidized; if $x > 3$, LYCB is reduced.

$$V = -\frac{E(Li_3YCl_3Br_3) - E(Li_xYCl_3Br_3) - (3-x)E(Li)}{3-x}$$

$Li_xYCl_3Br_3$ represents the most stable configuration (points on the convex line), and E represents the energy of the respective configurations.

The starting structures for LYCB were obtained from the literature[41] and our refinement. To comprehensively address halogen disorder, we randomized the halogen site occupation and conducted energy and geometry optimization, selecting the lowest-energy structure (Supplementary Fig. 38). Furthermore, to ensure the representation of all potential halogen and Y environments, additional LYCB structures

were examined. These included configurations with all the possible combinations of Cl–Br-formed octahedra (6Cl, 5Cl1Br, 4Cl2Br, 3Cl3Br, 2Cl4Br, 1Cl5Br and 6Br) alongside Y disorder in the 4*h* and 4*g* interstitial positions, as documented in previous literature[41] and our refinement, respectively. For the Li sublattice, the minimization of Coulombic interactions was performed for 100,000 permutations of Li distribution in interstitial positions at each Li concentration in the oxidation/reduction landscape (x in $Li_xYCl_3Br_3$). The 12 lowest-energy structures at each concentration step were selected for DFT optimization, forming the convex hulls. Tabulated details on the investigated structures are provided in Supplementary Table 4.

Data availability

Data supporting the findings from this work are available within this Article and its Supplementary Information. The data that support the plots within this paper are available via Zenodo at https://zenodo.org/records/15534634 (ref. 46).

References

41. Van Der Maas, E. et al. Investigation of structure, ionic conductivity, and electrochemical stability of halogen substitution in solid-state ion conductor $Li_3YBr_xCl_{6-x}$. *J. Phys. Chem. C* **127**, 125–132 (2023).
42. Toby, B. H. & Von Dreele, R. B. GSAS-II: the genesis of a modern open-source all purpose crystallography software package. *J. Appl. Crystallogr.* **46**, 544–549 (2013).
43. Kresse, G. & Furthmüller, J. Efficiency of ab-initio total energy calculations for metals and semiconductors using a plane-wave basis set. *Comput. Mater. Sci.* **6**, 15–50 (1996).
44. Blöchl, P. E. Projector augmented-wave method. *Phys. Rev. B* **50**, 17953–17979 (1994).
45. Perdew, J. P., Burke, K. & Ernzerhof, M. Generalized gradient approximation made simple. *Phys. Rev. Lett.* **77**, 3865–3868 (1996).
46. Cheng, Z. Source data for 'Beneficial redox activity of halide solid electrolytes empowering high-performance anodes in all-solid-state batteries'. *Zenodo* https://doi.org/10.5281/zenodo.15534634 (2025).

Acknowledgements

We acknowledge financial support from the National Growthfund program NXTGEN Hightech (M.W., Z.C., W.Z. and C.Z.), BatteryNL—Next Generation Batteries based on Understanding Materials Interfaces' project with project no. NWA.1389.20.089 (M.W. and A.K.L.) of the NWA research programme 'Research on Routes by Consortia (ORC)' funded by the Dutch Research Council (NWO), the Netherlands Organization for Scientific Research (NWO), under VICI grant no. 16122 (M.W. and V.L.) and under VENI grant no. 18123 (A.V.). We are grateful for the help of F. Ooms with the experiments, B. Boshuizen with the XPS measurements and Z. Lei with the SEM measurements.

Author contributions

M.W. and Z.C. conceived the project. Z.C., W.Z., Q.W. and C.Z. carried out the synthesis, XRD, NMR characterization and electrochemical measurements. Z.C. and L.B. carried out the XPS measurements and interpreted the data. A.K.L. and A.V. carried out the DFT and AIMD calculations. Y.L. and J.L. carried out the SEM measurements. All authors participated in discussing the results. Z.C. and M.W. prepared and revised the paper with inputs from all other authors.

Competing interests

The authors declare no competing interests.

Additional information

Supplementary information The online version contains supplementary material available at https://doi.org/10.1038/s41563-025-02296-6.

Correspondence and requests for materials should be addressed to Marnix Wagemaker.

Peer review information *Nature Materials* thanks Matteo Bianchini and the other, anonymous, reviewer(s) for their contribution to the peer review of this work.